Soft Matter

ROYAL SOCIETY OF CHEMISTRY

PAPER

View Article Online
View Journal | View Issue

Cite this: *Soft Matter*, 2024, **20**, 8260

Dynamics of phase-separated microdroplets near the contact line of evaporating all-aqueous drops†

Rahul Rai,‡ Maheshwar Gopu,‡ Senthan Pugalneelam Parameswaran, Tapan Chandra Adhyapak* and Dileep Mampallil*

Received 4th September 2024,
Accepted 1st October 2024

DOI: 10.1039/d4sm01056f

rsc.li/soft-matter-journal

Evaporation of multicomponent drops can induce liquid–liquid phase separation and spatial reconfiguration of phases. Here, we unveil several novel dynamics near the contact line of evaporating multicomponent drops containing polyethylene glycol and dextran. The interplay between background Marangoni flow and self-migration of nucleated microdroplets creates both unstable and stable equilibrium points. This leads to either continuous migration or stepwise advancement of microdroplets, influenced by random coalescence events. Tiny dextran microdroplets nucleating at the contact line can migrate toward the bulk only by growing in size with coalescence events. Our findings offer new insights into the fundamental understanding of evaporating multicomponent drops and factors influencing the spatial segregation of phases in evaporative liquid–liquid phase separation with implications in prebiotic biomolecular reactions to industrial applications.

Evaporation of drops, a process rich in physics, has profound implications in various applied processes.[1–6] A less explored system is the evaporating multicomponent drops. They undergo out-of-equilibrium processes, leading to liquid–liquid phase separation (LLPS),[7–11] particularly near the three-phase liquid–solid–air contact line, where significant evaporative fluxes occur.[12–18] In general, LLPS of aqueous two-phase systems[8,9] has applications in broad areas such as environmental remediation, water purification, synthetic biology, and biomedicine.[7,8,10,11] For example, LLPS can form microdroplets resembling membraneless organelles occurring in cells. LLPS by spontaneous evaporation has been shown to concentrate RNA molecules in compartments, as seen in protocells,[19–21] delineating the possible implications in the origin of life. Evaporative deposition of polymer components also has implications for the bottom-up construction of polymer-based systems with wide industrial applications.[22–24]

Evaporating multicomponent drops are complex systems containing intricate dynamics such as driving of nucleated microdroplets at the contact line through asymmetric interfacial stresses,[25–28] large-scale convection driven by strong recirculating solutal Marangoni flow,[12,14,20,29] and radial capillary flows.[4,30] In evaporative multiphase drop systems, hydrodynamic effects influence the spatial organization of the phases. For example, capillary and Marangoni background flows in multiphase sessile-drop evaporation in oil-coated surfaces could generate stagnation points stabilizing the hierarchically compartmentalized microdroplets.[21] In a different context, it was demonstrated that when partially immersed in oil (as an emulsion), evaporating multiphase polymer microdroplets separate into distinct phases.[31,32] In the widely used model system of polyethylene glycol (PEG) and dextran (DEX), sessile drop evaporation drives inward migrations of nucleated DEX microdroplets, resulting in a DEX-rich center (Fig. 1(a and b)) as also reported in previous studies.[12,20,28] Unfortunately, several complex dynamics of evaporating multicomponent drops are not well understood. For example, the interplay between the dynamics of the nucleated phases at the contact line and the background flow in the drop has been overlooked in previous studies.

Here, we unveil several previously unexplored dynamics surrounding the contact line during the evaporating PEG-DEX drop. We study the previously overlooked dynamics of nucleated DEX and, importantly, its interaction with the background flow. We show that DEX nuclei can migrate from the contact line to the bulk only by growing *via* coalescence, manifesting a stepwise motion with intermittent halts (Fig. 1(c and d)). Conversely, DEX nucleating slightly away moves continuously, either towards or away from the contact line, depending on its initial nucleation position (Fig. 1(e)). Our

Indian Institute of Science Education and Research Tirupati, Yerpedu P.O. PIN 517619, Tirupati, AP, India.
E-mail: adhyapak@iisertirupati.ac.in, dileep.mampallil@iisertirupati.ac.in

† Electronic supplementary information (ESI) available. See DOI: https://doi.org/10.1039/d4sm01056f

‡ Equal contribution.

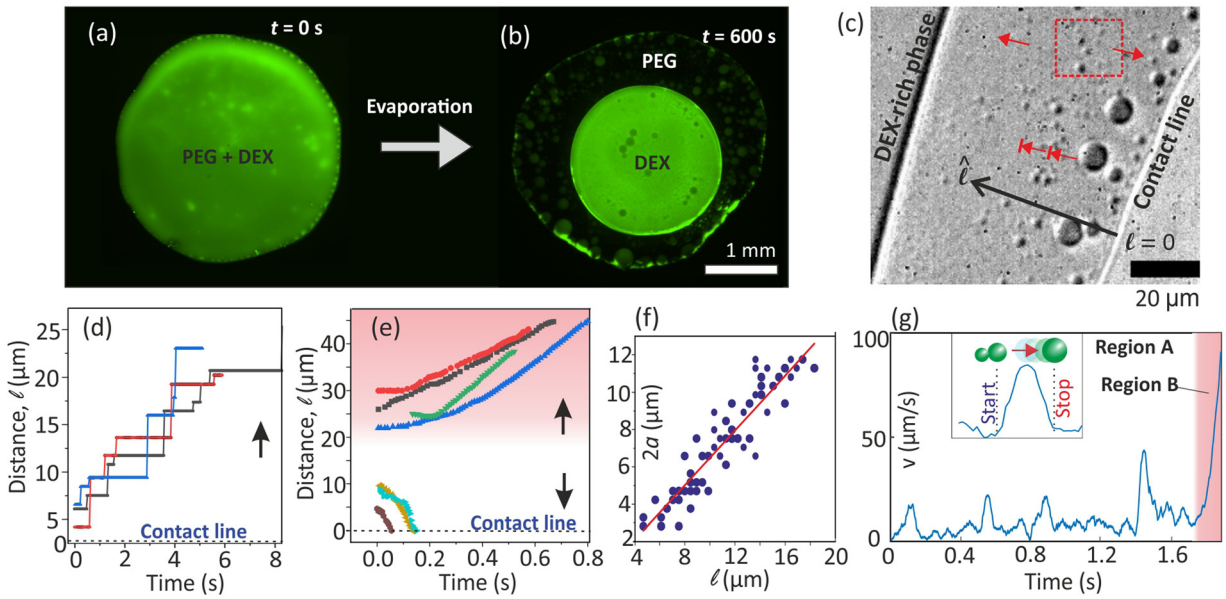

Fig. 1 (a) and (b) Bottom-view images of PEG-(FITC-DEX) drop. (c) DEX microdroplets at the contact line move stepwise (blunt-head arrows) toward the bulk upon coalescence. (d) Stepwise position change over time (Video S1, ESI†). (e) Tiny microdroplets (red dashed rectangle in (c)) nucleated away from the contact line move continuously towards the bulk or contact line, based on their nucleating point. (f) Size of stepwise migrating microdroplets as a function of distance from the contact line. (g) In the stepwise motion, velocity peaks upon a coalescence, and the resulting droplet halts at a new position. After multiple coalescence events, the resulting large droplet reaches a position where it migrates to the bulk without intermittent halting (marked as region B). The regions A & B are spatial regions near the contact line. Relative PEG : DEX concentration was 2 : 10 wt%.

analysis, supported by theory, reveals that these dynamics arise from the complex interplay between nucleated DEX and convective flow gradients near the contact line. Our findings offer broad insights into transport dynamics within evaporating multicomponent drops.

1 Experiments

In the experiments, we evaporated a polymer mixture drop of volume 1 μL deposited on an ethanol–oxygen plasma-cleaned dry glass slide at laboratory conditions (25 °C and humidity 50 ± 2%). The initial concentrations of individual polymers (DEX, M_w = 40 000 g mol^{-1} and PEG, M_w = 6000 g mol^{-1}) were prepared at 2–10 wt% in deionized water. We also used DEX tagged with FITC (fluorescein isothiocyanate; λ_{em} = 517 nm) for fluorescent imaging. The drop edge was imaged using an inverted fluorescence microscope (Nikon Eclipse Ti2) and cameras (Nikon DS-Qi2 and Vision Research Lab-110) at 24–200 frames per s with a maximum resolution of 0.33 μm per pix with 90× objective.

2 Results

2.1 Microdroplet dynamics observed near the contact line

Henceforth, the PEG-DEX sessile drop will be referred to as the "drop," while the micro-sized droplets that nucleate at the drop edge will be referred to as "microdroplet(s)." We imaged near the contact line, *i.e.*, within about 30 μm from the edge. The contact line is pinned on the substrate and does not move.

(i) The DEX microdroplets nucleating at the contact line can migrate away only by coalescence-induced growth and stepwise advancement (Fig. 1(d) and Video S1, ESI†). It is also reflected in their size distribution as shown Fig. 1(f). In Fig. 1(g), we display the velocity of a microdroplet in stepwise motion over time (Video S2, ESI†). Peaks indicate intermittent advancements of the microdroplet, rising from zero to a maximum post-coalescence before returning to near-zero velocity.

(ii) After coalescence cascades, resulting large microdroplets move continuously (region B in Fig. 1(g)) toward the bulk. The velocity of these continuously moving microdroplets increases over time.

(iii) Extremely small DEX microdroplets (diameter < 2 μm) nucleate slightly away from the contact line, possibly from a precursor film of denser DEX on the substrate. They move in the direction of the contact line or towards the bulk if they nucleate relatively closer to these corresponding regions, as depicted in Fig. 1(e) and (Video S1, ESI†).

Mainly, we observe that the nucleated DEX microdroplets move close to the substrate (liquid–solid interface). DEX stays near the substrate as its density (~1049 kg m^{-3}) is higher than that of the PEG-rich phase (~1017 kg m^{-3}).[28] We do not expect any pinning of the DEX microdroplets on the substrate as they are surrounded by liquid.

2.2 Understanding the microdroplet dynamics

When DEX nucleates, the drop edge undergoes a compositional change where it becomes predominantly composed of PEG. The gradient in the polymer concentration generates a corresponding gradient in the interfacial tension along the interface

between the microdroplets and the surrounding liquid.[12,28] The resulting Marangoni stress pushes the liquid on the microdroplet surface, assisting them to 'swim' in the opposite direction, *i.e.*, towards the drop center.[28]

Assuming that the interfacial tension, σ_{dl}, between the DEX microdroplet and surrounding liquid varies linearly, the Marangoni force of the microdroplets is given as,[28]

$$\mathbf{F}_M = F_M\hat{\ell} = \frac{\partial\sigma_{dl}}{\partial\ell}a^2\int_{S'}(\hat{\ell}\cdot\hat{t})\hat{t}\,dA', \qquad (1)$$

where the integral is over the non-dimensional surface S' of the microdroplet, dA' is a non-dimensional area element. They are non-dimensionalized by writing lengths in units of the droplet radius a. Furthermore, $\hat{\ell}$ & $\hat{t}$ the unit vectors along the inverse radius of the drop ($\ell = 0$ at the contact line, [see Fig. 1(c)]) and the local tangent to the droplet surface, respectively. The direction ℓ of $\mathbf{F}_M$ is inferred directly from the symmetry of the setup.

In the low Reynolds number limit, the hydrodynamic drag force on the droplet is, $\mathbf{F}_D = -\gamma\mathbf{v}_M$, where the drag coefficient γ of the microdroplet,[33] is linear in the radius a. Here, $\mathbf{v}_M = \mathbf{v} - \mathbf{u}_f$ is the velocity of the microdroplet relative to the background flow $\mathbf{u}_f$, while $\mathbf{v}$ is the velocity in the laboratory frame. Therefore, force-balance, $\mathbf{F}_M + \mathbf{F}_D = 0$, predicts a continuous motion of droplets with $\mathbf{v}_M \propto a$ as demonstrated by May *et al.*[28] (also see Fig. S3, ESI†). However, we show that this continuous motion occurs only for relatively large microdroplets at region B, after reaching there in a step-wise manner by a cascade of coalescence events. Interestingly, we also see that the measured microdroplet velocity ($\mathbf{v}$) increases continuously in region B. Below, we explain all these aspects considering the interplay between the convective flow $\mathbf{u}_f$ and the opposing Marangoni force $\mathbf{F}_M$.

The low surface tension towards the drop edge at the drop–air interface induces a large-scale Marangoni convective recirculation flow inside the drop.[20,28] Its velocity $\mathbf{u}_f = -u_f\hat{\ell}$ is radially outward near the drop–substrate interface. Writing $\gamma = C_{HR}a$, where C_{HR} is the constant in Hadamard–Rybczynski drag equation,[33] the lab frame velocity of the microdroplets is read from eqn (1), as

$$\mathbf{v} = \left[\frac{\partial\sigma_{dl}}{\partial\ell}\frac{a}{C_{HR}}\int_{S'}(\hat{\ell}\cdot\hat{t})^2 dA' - u_f\right]\hat{\ell}. \qquad (2)$$

The droplet moves radially inward step by step if its radius a increases through coalescence, and the external flow velocity $\mathbf{u}_f$ also increases inward radially. This scenario leads to multiple consecutive equilibrium positions with $\mathbf{v} = 0$.

The strong Marangoni flow generated at the liquid–air interface of the drop expands in its bulk as a circulating flow. We expect gradients in the flow strength, especially near the corners, as they are far away from the circulation path. Although it is experimentally challenging to visualize this gradient in the small region near the drop edge, numerical simulations of Marangoni convective flow do reveal it.[34–36] We also performed numerical simulations (see ESI†), excluding

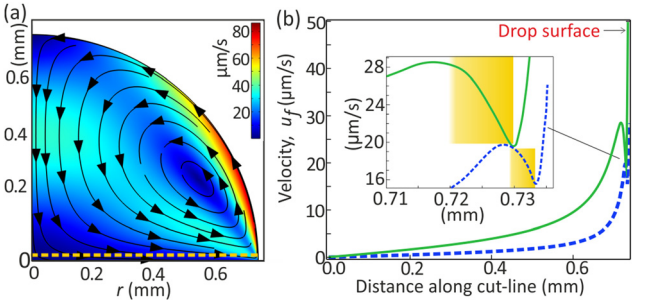

Fig. 2 (a) The simulated large Marangoni recirculating flow inside the drop. (b) The magnitude of the flow along the dashed cut-line drawn in (a) at two different heights z = 3 (dashed line) & 10 μm from the substrate. The region of drag force producing stepwise motion is highlighted in the inset.

nucleation processes and complexities caused by microdroplets near the contact line. Such a flow can occur when surface tension is relatively higher towards the apex of the drop, which is a scenario usually occurring by solutal or thermal gradients. Although the flow in our drop is driven by solutal Marangoni stress, our simulations easily produced the correct flow direction, as shown in Fig. 2(a), through evaporatively generated thermal gradients ∇T, which induce interfacial stress $(d\sigma/dT)\nabla T$. The circulating flow pattern persists even under very large interfacial stresses, similar to solutal Marangoni flow (Fig. S4, ESI†), as demonstrated in other studies.[34–36] The interaction between the DEX microdroplets and the background flow is independent of the specific origin of the flow.

Fig. 2(b) shows the numerically calculated flow magnitude just above the substrate. Moving radially inward (along $\hat{\ell}$) from the contact line, the fluid velocity strength increases (highlighted in the inset) creating a barrier for self-migrating microdroplets along ℓ. This increased flow strength transitions to a decrease towards the drop center.

The flow strength varies along the horizontal cutline due to the drop's shape, with reduced fluid velocity near the drop's edge. This is illustrated by the dark blue band emanating from the drop edge in Fig. 3(a), consistent with numerical calculations by others for thermal and solutal Marangoni flows.[34–36]

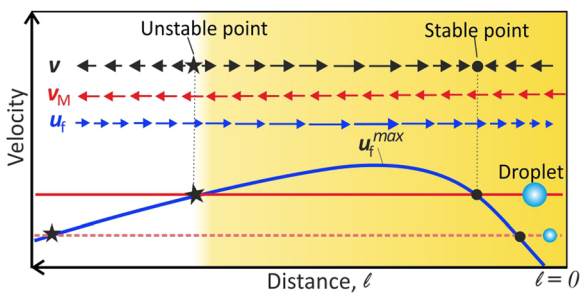

Fig. 3 Illustrated velocities of background convective flow ($\mathbf{u}_f$; blue lines) and microdroplets ($\mathbf{v}_M$; red lines). Unstable (★) and stable (●) equilibrium points are formed at $\mathbf{v}_M + \mathbf{u}_f = 0$. Arrows indicate velocity magnitude and direction for the large droplet. When the small droplet enlarges, its (dashed line) $\mathbf{v}_M$ increases (solid line) resulting in smaller extent of the stable equilibrium region (highlighted yellow).

The effect of the corner depends upon the flow-circulation position (Fig. S5, ESI†) and appears to be stronger with decreasing contact angle of the drop.[35,37] Experimentally, the circulation appears to be closer to the drop edge where the surface tension gradients exist at the drop–air interface.

The peak-like variation of $\mathbf{u}_f$ near the contact line has an important consequence: the condition $\mathbf{v} = \mathbf{v}_M + \mathbf{u}_f = \mathbf{0}$ produce locations of stable and unstable equilibrium. It is schematically illustrated in Fig. 3. Now we can explain all the droplet dynamics observed near the contact line.

The existence of the unstable equilibrium position can explain why the very small DEX microdroplets formed from the precursor film, away from the contact line, move continuously. When microdroplets nucleate between the unstable and stable regions, they flow towards the contact line, as $\mathbf{u}_f(\ell) > \mathbf{v}_M$. Conversely, microdroplets, nucleating beyond the unstable equilibrium, flow directly towards the bulk along the substrate as $\mathbf{v}_M > \mathbf{u}_f(\ell)$ (Video S1, ESI†).

On the other hand, due to the flow barrier as highlighted region Fig. 2(b)-inset or Fig. 3, the small microdroplets nucleating at the contact line can migrate to the bulk only by coalescence-induced size increase. Each coalescence causes $\mathbf{v}_M > \mathbf{u}_f(\ell)$, and results in the migration of the microdroplet to the next stable equilibrium position where $\mathbf{v}_M + \mathbf{u}_f(\ell) = \mathbf{0}$.

After multiple coalescence events, the resulting large daughter droplet has $\mathbf{v}_M > \mathbf{u}_f^{max}$, where $\mathbf{u}_f^{max}$ is the maximum flow velocity (see Fig. 3). At this stage, no stable equilibrium is possible, and therefore, the microdroplet flows continuously towards the bulk (as reported in ref. 28). However, the droplet velocity steadily increases (region B in Fig. 1(g)) since the convective flow velocity ($\mathbf{u}_f$) decreases towards the drop center, as inferred in Fig. 2(b).

Apart from the migration of the DEX microdroplets near and parallel to the substrate, rarely do we observe that the tiny microdroplets get trapped in the large background recirculating flow. They move upward near the liquid–air interface and flow back to the contact line, similar to the dynamics described in PEG-DEX drops[28] and also in the Marangoni ring formation in evaporating water–glycerol drops.[29]

2.3 Velocity change during individual coalescence

In Fig. 1(g), each coalescence event shifts a resting microdroplet to a new position, showcasing a velocity pattern starting from zero, peaking, and then returning to zero. Concurrently, the shape of the coalescing microdroplets is found to undergo a systematic pattern change, as shown in Fig. 4(a): first, the two merging spheres are connected through a neck which grows until the shape becomes an ellipsoid;[38,39] subsequently, relaxing to a final larger sphere.[40] In the following, for simplicity, we assume that the neck growth and the relaxation back to the sphere happens sequentially and independent of each other.

A correlation between the velocity peak and the shape change can be predicted from the time variation of the factor $\phi = F_M/(a^2\partial_\ell\sigma_{dl}) = \int_{S'}(\hat{\ell}\cdot\hat{t})^2 dA'$ of eqn (1). Being a non-dimensonalized factor, ϕ depends only on the shape of the surface S'. For spheres coalescing along the radial direction,

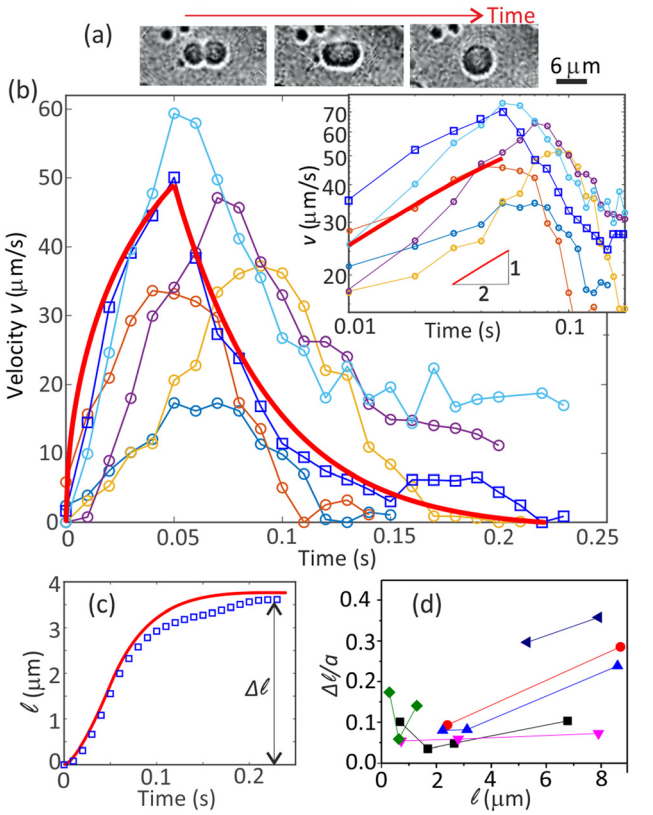

Fig. 4 (a) Shape change during the coalescence of two microdroplets. (b) Experimental velocity ($\mathbf{v}$) peaks during coalescence events (also Fig. 1(g)). The solid red curve is from theory and represents one of the experimental curves (squares). The inset shows $t^{1/2}$ growth of the velocity. (c) The distance traveled by the drop upon a coalescence. The plot corresponds to the data with connected open squares in (b). The solid red curve is theoretically calculated. (d) The scaled step length ($\Delta\ell/a$) increases towards small and large ℓ, where corresponding small m values exist. The uncertainties in the values of v and ℓ correspond to at least one pixel. Given a resolution of 0.33 μm per pixel, this translates to uncertainties of at least 2 μm s^{-1} for v and 0.33 μm for ℓ.

ϕ peaks when S' is ellipsoidal (because ellipsoids aligning along $\hat{\ell}$ maximizes $\left(\hat{\ell}\cdot\hat{t}\right)^2$ for most part of S'). Assuming a to be an average linear size of the combined microdroplets, we infer that the time dependence of F_M is predominantly due to that of ϕ. Therefore, it follows from above that F_M, too, peaks at the ellipsoidal shape, qualitatively explaining the peak in the relative velocity $\mathbf{v}_M$ (the peaking of ϕ can easily be demonstrated in a numerical experiment of coalescence of two 2D droplets as shown in the ESI†).

The effect of the background flow $\mathbf{u}_f$ to the above analysis can be deduced from eqn (2) which implies that during a coalescence, $\dot{\mathbf{v}}_M \equiv \dot{\mathbf{v}} - \dot{\mathbf{u}}_f = aD\dot{\phi}\hat{\ell}$, where $D = \partial_\ell\sigma_{dl}/C_{HR}$. Identifying $\dot{\mathbf{u}}_f = -\dot{u}_f\hat{\ell}$ as $-m\mathbf{v}$, with $m = du_f/d\ell$ the slope of u_f in the linear region [Fig. 2(b)], we find the lab-frame velocity $\mathbf{v}$ to evolve as:

$$\frac{d\mathbf{v}}{dt} + m\mathbf{v} = aD\frac{d\phi}{dt}\hat{\ell} \qquad (3)$$

The factors D and m are experimentally estimable (see Appendix). The coalescence of two drops, or the factor ϕ, follows a dynamics characterized by the fast growth of the neck radius initially as $t \ln t$ followed by $t^{1/2}$.[38,39,41] Our experiments cannot capture the early time $t \ln t$ dynamics. After the initial growth, the ellipsoidal drop recovers to the final spherical shape in a nearly exponential manner.[40] With the corresponding forms of ϕ, eqn (3) predicts the theoretical solution $v(t)$ (see Appendix), which is plotted in Fig. 4(b) (solid red line), whereas the displacement during a coalescence, $\ell(t) = \int_0^t v(\tau)\mathrm{d}\tau$, is plotted in Fig. 4(c) (solid red line).

The experimental data was obtained by tracking the microdroplets near the contact line within a range of about 20 μm. It is achieved by a well-established tracking algorithm[42] available publicly (included in the data in ESI†). The experimental velocities and displacement are also shown alongside in Fig. 4(b and c), respectively. While the experimental plots are in qualitative agreement with the exponential decay, the $t^{1/2}$ growth dynamics is evident from both theory and experiments [inset, Fig. 4(b)]. Accordingly, displacements $\ell(t)$ have a good agreement between theory and experiments, showing deviations only slightly in the decay regions [Fig. 4(c)].

The strength of the background flow gradient (or slope m) decreases near and far from the contact line as inferred from Fig. 2(b) inset (also Fig. S6, ESI†). A decrease in the gradient allows the microdroplet to step a longer distance. Thus, we expect $\Delta\ell$ to have larger values very close to and far away from the contact line, also as seen in Fig. 4(d). A similar effect can be seen for $\mathbf{v}$ during the coalescence-induced motion (Fig. S7, ESI†). Our analytical model also predicts this trend for $\Delta\ell$ and a peak of v during the coalescence (see Appendix and Fig. S8 and S9, ESI†).

Based on our model, we can anticipate certain microdroplet behavior during coalescence. When m is large, the condition $\mathbf{v}_\mathrm{M} + \mathbf{u}_\mathrm{f}(\ell) = 0$ may occur before complete shape relaxation to a sphere. In such instances, the decreasing $\mathbf{v}_\mathrm{M}$ with shape relaxation must make $\mathbf{v}$ negative, causing a slight droplet retraction (see Appendix and Fig. S10, ESI†).

In our discussions, we have omitted factors such as the weak evaporation-driven capillary flow,[4] viscosity gradient near the contact line, or effects of surrounding microdroplets.

3 Summary

In summary, we show that DEX nuclei, forming at the contact line of evaporating PEG-DEX drop, can migrate towards the bulk only by growing with random coalescence events. The interplay between the increasing size and gradient in the background flow strength leads to stepwise migration of these DEX nuclei. Understanding the interplay between the transport of nucleated phases and the background flows in the evaporating multiphase drops allows the development of strategies to control the self-organization of the phases. Thus, our findings provide valuable fundamental insights and opportunities for developing control of evaporation of multicomponent drops, LLPS-based membraneless compartment systems,[19–21] and multiphase polymer systems of industrial applications such as inkjet printing,[22,23] fabrication of biomaterials,[24] and biomedical applications.[43]

Author contributions

R. R., M. G., and S. P. P. performed the experiments, analyzed the data. DM designed the project, and TCA and DM performed the modeling and wrote the manuscript.

Data availability

The data supporting this article have been included as part of the ESI.†

Conflicts of interest

The authors declare no conflicts of interest.

Appendix

Analytical model of coalescence-induced motion

Neglecting the inertial effects we have the equation of motion, $\mathbf{F}_\mathrm{D} + \mathbf{F}_\mathrm{M} = 0$. Or,

$$-C_\mathrm{HR} a \mathbf{v}_\mathrm{M} + \frac{\partial \sigma_\mathrm{dl}}{\partial \ell} a^2 \left(\int_{S'} (\hat{\ell} \cdot \hat{t})^2 \mathrm{d}A' \right) \hat{\ell} = 0, \tag{4}$$

The velocity of the DEX nuclei in the lab frame is given as

$$\mathbf{v} = \mathbf{v}_\mathrm{M} + \mathbf{u}_\mathrm{f} \tag{5}$$

where $\mathbf{u}_\mathrm{f}$ is the co-flow velocity. We can rewrite eqn (4) taking time derivative as,

$$\frac{\mathrm{d}\mathbf{v}}{\mathrm{d}t} - \frac{\mathrm{d}\mathbf{u}_\mathrm{f}}{\mathrm{d}t} = aD \frac{\mathrm{d}\phi}{\mathrm{d}t} \hat{\ell} \tag{6}$$

where, $D = \dfrac{\partial \sigma_\mathrm{dl}}{\partial \ell} \dfrac{1}{C_\mathrm{HR}}$ and $\phi = \left(\int_{S'} (\hat{\ell} \cdot \hat{t})^2 \mathrm{d}A' \right)$, which is a numerical factor depending upon the shape of the droplet during coalescence. We have the following directional relationships: $\mathbf{v} = v\left(\hat{\ell}\right)$, $\mathbf{u}_\mathrm{f} = u_\mathrm{f}\left(-\hat{\ell}\right)$, and $\mathbf{v}_\mathrm{M} = v_\mathrm{M}\left(\hat{\ell}\right)$. Writing $\mathrm{d}\mathbf{u}_\mathrm{f}/\mathrm{d}t = -(\mathrm{d}u_\mathrm{f}/\mathrm{d}\ell)(\mathrm{d}\ell/\mathrm{d}t)\hat{\ell} = -mv\hat{\ell}$, where m is the gradient (slope) of the flow, results in eqn (3).

The coalescence process involves two parts: first is the merging of two droplets to form an ellipsoidal droplet. The second part is the relaxation of the ellipsoidal droplet to a final spherical one.

Case 1: initial merging of two droplets. The neck connecting the two droplets grows as $(t/\tau_0)^{1/2}$, where τ_0 is a time constant.[41] It is in the order of the inertial-capillary time $\tau_\mathrm{ic} = (\delta\rho a^3/\sigma_\mathrm{dl})^{1/2}$ (ref. 39).

Table 1 The asteric (*) for b_0 indicates the assumption, $\tau_0 = \tau_{ic}$

	Estimate	In Fig. 4(c)
m	2.5 s^{-1}	5.0 s^{-1}
b_0	540* $s^{-3/2}$	49 $s^{-3/2}$
b	10×10^{-4} m s^{-2}	8.4×10^{-4} m s^{-2}
τ_{vc}	0.05 s	0.05 s

We can consider $\phi \sim (t/\tau_0)^{1/2}$ and eqn (3) can be rewritten as,

$$\frac{dv}{dt} + mv = ab_0\frac{1}{\sqrt{t}} \quad (7)$$

where $b_0 = D/2\sqrt{\tau_0}$.

The solution of eqn (7) can be obtained as,

$$v(t) = \frac{ab_0 e^{-mt}\Gamma(1/2, -mt)}{(-m)^{1/2}} + C_1 e^{-mt}, \quad (8)$$

where Γ is the incomplete gamma function. The integration constant C_1 is zero as $v = 0$ at $t = 0$.

Case 2: relaxation of the ellipsoidal droplet. The relaxation of the ellipsoidal droplet occurs an exponential manner as $e^{-t/\tau_{vc}}$, where $\tau_{vc} = \mu a/\sigma_{dl}$ is the visco-capillary time (ref. 40), with μ is the viscosity of the continuous fluid in the drop. Here, we can consider that $\phi \sim e^{-t/\tau_{vc}}$.

Eqn (3) can be written as,

$$\frac{dv}{dt} + mv = -be^{-t/\tau_{vc}}, \quad (9)$$

where $b = D\sigma_{dl}/\mu$.

The solution of eqn (9) can be obtained as,

$$v(t) = \frac{be^{-t/\tau_{vc}}}{\tau_{vc}^{-1} - m} + C_2 e^{-mt} \quad (10)$$

The integration constant can be obtained from the boundary condition, $v = v_{peak}$ at $t = 0$, where v_{peak} is the velocity at the end of the first merging phase (case 1). Finally, we obtain,

$$v(t) = \frac{b}{\tau_{vc}^{-1} - m}\left(e^{-t/\tau_{vc}} - e^{-mt}\right) + v_{peak}e^{-mt}. \quad (11)$$

Estimating the parameters m, b_0, b, and τ_{vc}. The value of m was estimated as 2.5 s^{-1} from the slope of the data v *versus* distance, l. Similarly, the value of D was estimated as 10 s^{-1} from the data v *versus* a.

Taking $a = 5$ μm, $\mu = 10$ mPa s, $\sigma_{dl} = 1$ μN m^{-1}, and $\delta\rho = 32$ kg m^{-3}, we estimate the parameters and shown in the Table 1.

We used the values shown in the Table to plot a representative theoretical curve for one of the experimental data plotted in Fig. 4(c) in the manuscript. The droplet radius was $a = 4.7$ μm. The time period for drop merging was 0.05 s (the time point where the velocity peak appears). Thus, eqn (8) was calculated for a duration 0–0.05 s. Eqn (11) was calculated until the velocity becomes zero.

Distance ℓ upon each coalescence. We can integrate eqn (8) and (11) for the duration of the droplet movement to obtain the distance traveled by the droplet. It also gives the step length $\Delta\ell$.

Special case 1. It is possible that the relaxation of the microdroplet is complete before it meets the condition $\mathbf{v}_M + \mathbf{u}_f = \mathbf{0}$. It means that, upon completion of the relaxation, the droplet has a constant Marangoni force (due to the constant final radius). Thus, the equation of motion becomes,

$$\frac{dv}{dt} + mv = 0, \quad (12)$$

resulting in an exponential decay of the velocity as,

$$v(t) = v_0 e^{-mt} \quad (13)$$

where v_0 is the initial velocity for the constant Marangoni force regime.

Special case 2. It is also possible that upon coalescence, the daughter droplet meets the condition $\mathbf{v}_M + \mathbf{u}_f = \mathbf{0}$ before its complete shape relaxation. It means that a non-spherical droplet comes to a halt. However, as the relaxation continues, the shape becomes spherical, and the Marangoni force decreases slightly. During this decrease, the droplet moves backward slightly to meet the condition $\mathbf{v}_M + \mathbf{u}_f = \mathbf{0}$. Such a scenario can occur at large flow gradient (m) values as plotted in Fig. S10 (ESI†).

Acknowledgements

DM and TCA acknowledge grants CRG/2020/003117 and CRG/2021/004759, respectively, from the Science and Engineering Research Board (India).

Notes and references

1 S. K. Wilson and H.-M. D'Ambrosio, *Annu. Rev. Fluid Mech.*, 2023, **55**, 481–509.
2 D. Mampallil and H. B. Eral, *Adv. Colloid Interface Sci.*, 2018, **252**, 38–54.
3 H. Hu and R. G. Larson, *J. Phys. Chem. B*, 2006, **110**, 7090–7094.
4 A. G. Marín, H. Gelderblom, D. Lohse and J. H. Snoeijer, *Phys. Rev. Lett.*, 2011, **107**, 085502.
5 S. Shiri, S. Sinha, D. A. Baumgartner and N. J. Cira, *Phys. Rev. Lett.*, 2021, **127**, 024502.
6 W. D. Ristenpart, P. G. Kim, C. Domingues, J. Wan and H. A. Stone, *Phys. Rev. Lett.*, 2007, **99**, 234502.
7 L.-P. Bergeron-Sandoval, N. Safaee and S. W. Michnick, *Cell*, 2016, **165**, 1067–1079.
8 M. Iqbal, Y. Tao and S. Xie, *et al.*, *Biol. Proced. Online*, 2016, **18**, DOI: 10.1186/s12575-016-0048-8.
9 C. P. Brangwynne, P. Tompa and R. V. Pappu, *Nat. Phys.*, 2015, **11**, 899–904.
10 C. D. Keating and R. V. Pappu, *J. Phys. Chem. B*, 2021, **125**, 12399–12400.
11 A. A. M. André and E. Spruijt, *Int. J. Mol. Sci.*, 2020, **21**, 18.
12 B.-U. Moon, L. Malic, K. Morton, M. Jeyhani, A. Elmanzalawy, S. S. H. Tsai and T. Veres, *Langmuir*, 2020, **36**, 14333–14341.
13 C. H. Ooi, E. Bormashenko, A. V. Nguyen, G. M. Evans, D. V. Dao and N.-T. Nguyen, *Langmuir*, 2016, **32**, 6097–6104.

14 C. Diddens, H. Tan, P. Lv, M. Versluis, J. G. M. Kuerten, X. Zhang and D. Lohse, *J. Fluid Mech.*, 2017, **823**, 470–497.
15 H. Tan, C. Diddens, P. Lv, J. G. M. Kuerten, X. Zhang and D. Lohse, *Proc. Natl. Acad. Sci. U. S. A.*, 2016, **113**, 8642–8647.
16 Y. Li, P. Lv, C. Diddens, H. Tan, H. Wijshoff, M. Versluis and D. Lohse, *Phys. Rev. Lett.*, 2018, **120**, 224501.
17 H. Sadafi, R. Rabani, S. Dehaeck, H. Machrafi, B. Haut, P. Dauby and P. Colinet, *Colloids Surf., A*, 2020, **602**, 125052.
18 Y. Li, P. Lv, C. Diddens and D. Lohse, *J. Fluid Mech.*, 2022, **946**, A37.
19 H. M. Fares, A. E. Marras, J. M. Ting, M. V. Tirrell and C. D. Keating, *Nat. Commun.*, 2020, **11**, 5423.
20 W. Guo, A. B. Kinghorn, Y. Zhang, Q. Li, A. D. Poonam, J. A. Tanner and H. C. Shum, *Nat. Commun.*, 2021, **12**, 1–13.
21 C. Qi, X. Ma, Q. Zeng, Z. Huang, S. Zhang, X. Deng, T. Kong and Z. Liu, *Nat. Commun.*, 2024, **15**, 1107.
22 U. S. B. J. de Gans and P. C. Duineveld, *Adv. Mater.*, 2016, **16**, DOI: **10.1186/s12575-016-0048-8**.
23 J. F. Dijksman, P. C. Duineveld, M. J. J. Hack, A. Pierik, J. Rensen, J.-E. Rubingh, I. Schram and M. M. Vernhout, *J. Mater. Chem.*, 2007, **17**, 511–522.
24 S. M. Park and D. K. Yoon, *Mater. Horiz.*, 2024, **11**, 1843–1866.
25 S. Michelin, *Annu. Rev. Fluid Mech.*, 2023, **55**, 77–101.
26 C. C. Maass, C. Krüger, S. Herminghaus and C. Bahr, *Annu. Rev. Condens. Matter Phys.*, 2016, **7**, 171–193.
27 Z. Izri, M. N. van der Linden, S. Michelin and O. Dauchot, *Phys. Rev. Lett.*, 2014, **113**, 248302.
28 A. May, J. Hartmann and S. Hardt, *Soft Matter*, 2022, **18**, 6313–6317.
29 L. Thayyil Raju, C. Diddens, Y. Li, A. Marin, M. N. van der Linden, X. Zhang and D. Lohse, *Langmuir*, 2022, **38**, 12082–12094.
30 R. D. Deegan, O. Bakajin, T. F. Dupont, G. Huber, S. R. Nagel and T. A. Witten, *Phys. Rev. E: Stat. Phys., Plasmas, Fluids, Relat. Interdiscip. Top.*, 2000, **62**, 756–765.
31 M. Kumar, M. Gopu, S. Pugalneelam Parameswaran, P. Joshi and D. Mampallil, *JCIS Open*, 2024, **13**, 100101.
32 M. Gopu and D. Mampallil, *Phys. Fluids*, 2022, **34**, 102110.
33 G. L. Leal, *Advanced Transport Phenomena*, Cambridge University Press, Cambridge, 2007.
34 R. van Gaalen, H. Wijshoff, J. Kuerten and C. Diddens, *J. Colloid Interface Sci.*, 2022, **622**, 892–903.
35 M. R. Barmi and C. D. Meinhart, *J. Phys. Chem. B*, 2014, **118**, 2414–2421.
36 B. Bozorgmehr and B. T. Murray, *ACS Omega*, 2021, **6**, 12577–12590.
37 Z. Pan, S. Dash, J. A. Weibel and S. V. Garimella, *Langmuir*, 2013, **29**, 15831–15841.
38 J. Eggers, J. R. Lister and H. A. Stone, *J. Fluid Mech.*, 1999, **401**, 293–310.
39 X. Xia, C. He and P. Zhang, *Proc. Natl. Acad. Sci. U. S. A.*, 2019, **116**, 23467–23472.
40 H.-X. Zhou, *J. Chem. Phys.*, 2021, **155**, 145102.
41 L. Duchemin, J. Eggers and C. Josserand, *J. Fluid Mech.*, 2003, **487**, 167–178.
42 J. C. Crocker and D. G. Grier, *J. Colloid Interface Sci.*, 1996, **179**, 298–310.
43 Y. Chao and H. C. Shum, *Chem. Soc. Rev.*, 2020, **49**, 114–142.

